

Accelerated molecular vibrational decay and suppressed electronic nonlinearities in plasmonic cavities through coherent Raman scattering

Lukas A. Jakob,^{*} William M. Deacon,^{*} Rakesh Arul[✉], Bart de Nijs, Niclas S. Mueller[✉], and Jeremy J. Baumberg^{✉†}
Nanophotonics Centre, Cavendish Laboratory, University of Cambridge, Cambridge CB3 0HE, United Kingdom

 (Received 19 August 2022; revised 21 March 2024; accepted 26 March 2024; published 2 May 2024)

Molecular vibrations and their dynamics are of outstanding importance for electronic and thermal transport in nanoscale devices as well as for molecular catalysis. The vibrational dynamics of <100 molecules are studied through three-color time-resolved coherent anti-Stokes Raman spectroscopy using plasmonic nanoantennas. This isolates molecular signals from four-wave mixing (FWM) while using exceptionally low nanowatt powers to avoid molecular damage via single-photon lock-in detection. FWM is found to be strongly suppressed in nanometer-wide plasmonic gaps compared to plasmonic nanoparticles. Simultaneous time-resolved incoherent anti-Stokes Raman spectroscopy allows us to separate the contributions of vibrational population decay (T_1) and dephasing (T_2). With increasing illumination intensity, the ultrafast vibrational dephasing rates of biphenyl-4-thiol molecules are accelerated at least tenfold, while phonon population decay rates remain constant. The extreme plasmonic field enhancement within nanogaps opens up prospects for measuring single-molecule vibrationally coupled dynamics and diverse molecular optomechanics phenomena.

DOI: [10.1103/PhysRevB.109.195404](https://doi.org/10.1103/PhysRevB.109.195404)

I. INTRODUCTION

The intense optical fields elicited by plasmonic nanostructures allow routine access to spectra of single or a few molecules under ambient conditions [1–3]. This starts to open prospects for understanding the dynamics and chemistry of individual molecules in real time. Using high-speed imaging, it is possible to track the dynamics of a few molecules on the microsecond scale [4] using surface-enhanced Raman spectroscopy (SERS). However, pushing the time resolution down to the scale of molecular vibrations (picoseconds) with ultrafast time-resolved spectroscopies has proven extremely difficult [5,6]. Early measurements of molecular phonon dynamics through surface-enhanced coherent anti-Stokes Raman spectroscopy (SE-CARS) on single nanostructures suggested great promise [7–9]; however, since then, little progress has been made [5,10]. Molecular dynamics studied recently in ultrafast pump-probe spectroscopy of spontaneous SERS instead averages over many molecules [11,12].

Single- and few-molecule SE-CARS and SERS measurements are possible only due to the high field intensities and Raman enhancements achieved when exciting plasmonic cavities with ultrafast pulses [13]. However, an unwanted consequence of these extreme peak fields is a rapid increase in nanoscale damage compared to continuous wave mea-

surements [5,14–16], which modifies both the metallic and molecular components of the system. This is particularly a problem for electronically resonant molecules, which enhance signals but are damaged much more easily. As a result, time-resolved SE-CARS (trCARS) measurements, which demand the structure to be stable throughout, become impractical. Although the damage thresholds are known, the mechanisms behind this damage remain unresolved [17], being most likely due to nonequilibrium heating and optical forces acting directly on the surface gold atoms [15,18].

The second problem with SE-CARS is the large overlapping four-wave mixing (FWM) signal due to electronic FWM [19–21]. Claims that the fast timescale of FWM enables separation of this from SE-CARS [22] assume that the molecular vibrational lifetime is much longer than the electronic lifetimes, which, as we demonstrate below, is not the case for molecules under strong confinement.

To circumvent these problems, we develop a three-color trCARS scheme to measure the reduction in dephasing lifetimes of exemplar biphenyl-4-thiol molecules in tightly confined plasmonic cavities. Surprisingly, the electronic FWM contribution is now found to be small ($<10\%$) despite the penetration of light into the metal, enabling extraction of SE-CARS signatures from ~ 100 molecules. Furthermore, we combine trCARS measurements with time-resolved incoherent anti-Stokes Raman spectroscopy (trIARS), which probes an incoherent phonon population with spontaneous anti-Stokes scattering, and has previously been used to study carbon nanomaterials [23–26]. Using a newly developed single-photon timestamping technique [27], we can simultaneously measure coherent trCARS [Fig. 1(a)] and spontaneous trIARS [Fig. 1(b)] on individual nanostructures at sub- μ W powers to independently probe the coherence (T_2) and population lifetimes (T_1), respectively [28]. This

^{*}These authors contributed equally to this work.

[†]Corresponding author: jjb12@cam.ac.uk

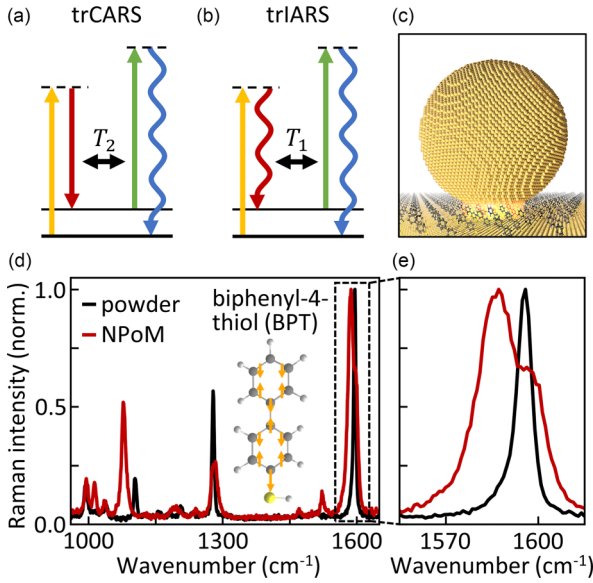


FIG. 1. Raman scattering from biphenyl-4-thiol (BPT) in plasmonic nanocavities. Excitation scheme of (a) coherent anti-Stokes Raman scattering (trCARS) and (b) spontaneous incoherent anti-Stokes Raman scattering (trIARS). Spontaneous or incoherent (wavy arrow) vs stimulated or coherent (straight arrow) processes. (c) Nanoparticle-on-mirror (NPoM) geometry with molecular layer in nanogap. (d) Continuous-wave Raman spectrum of BPT powder (black) compared with SERS from BPT in the NPoM cavity (red). Inset: BPT molecule with arrows indicating the coupled ring vibrational mode (1585 cm^{-1}). (e) Detailed view of coupled ring vibration in BPT. Binding to the gold surface splits and broadens the vibrational line.

ultrasensitive three-color coherent anti-Stokes Raman spectroscopy (CARS) scheme thus allows us to independently determine the population decay and dephasing in few-molecule plasmonically enhanced systems, giving insights into phonon dynamics of molecules tightly coupled to metallic interfaces.

II. EXPERIMENTAL SETUP

Nanoparticle-on-mirror (NPoM) plasmonic nanocavities confine light to the nanometer-scale gap between a metallic nanoparticle and the underlying metal substrate [Fig. 1(c)] [29,30]. These structures are also known as metal-insulator-metal (MIM) waveguides, or particle-on-film structures. This platform for few-molecule vibrational spectroscopy traps optical fields to zeptoliter volumes, filled only by the molecules under study [31]. The NPoM geometry has facilitated exploration of many processes through SERS including the movement of single atoms, tracking nanoelectrochemistry, and molecular optomechanical coupling [15,32–35].

We utilize NPoM structures built from 80-nm gold nanoparticles separated from a gold substrate by a self-assembled monolayer (SAM) of biphenyl-4-thiol (BPT) (see Appendix A). To improve the outcoupling of the CARS signal and increase sample stability, the NPoM structures are covered with a thin film of PMMA which enhances the NPoM scattering resonance in the signal range around 650 nm (see

Fig. S1 of the Supplemental Material [36] [37]. Due to the molecular binding to gold surface atoms, the molecular SERS spectra are modified compared to their powder Raman spectrum [Fig. 1(d)]. Notably, the coupled ring mode at 1585 cm^{-1} [Fig. 1(e)] splits into two modes with separation 13 cm^{-1} and is broadened in the NPoM structure compared to the powder spectrum. However, this effect is only observable with narrow-linewidth continuous-wave lasers since picosecond-pulsed lasers have a larger spectral bandwidth, thus broadening the Raman peak linewidth.

Nanoparticles are automatically located and characterized using a custom-built reflective dark-field microscope, prior to each trCARS measurement [Fig. 2(a)]. In our implementation, three temporally and spectrally independent input beams are required in the pulse train: the pump (set as $t = 0$, λ_p), the Stokes ($t = \tau_S$, λ_S), and the probe pulses ($t = \tau_x$, λ_x) [Fig. 2(b)]. The spectral shift between the pump and the Stokes pulse is chosen to populate the vibrational mode under study with frequency ω_v (here $\omega_p - \omega_S = \omega_v = 1585\text{ cm}^{-1}$). To achieve this, a tuneable pulse from an optical parametric oscillator (OPO) provides λ_p and λ_x while the 820-nm pump laser provides λ_S . Bandpass filtering sets all pulses to 0.5 ps pulse width (1.5 nm spectral width) to balance spectral and temporal resolution and reduce damage. The spectrum of $\lambda_{p,x}$ is selected from the 10-nm-wide OPO pulse by independently tuned bandpass filters. Pulse energies are kept low enough to avoid damage to the NPoM constructs (average powers $<4\text{ }\mu\text{W }\mu\text{m}^{-2}$, pulse energies $<50\text{ fJ}$). After filtering out the laser pulses from the emitted light, signals are detected either by a spectrometer or by a single-photon detector for single-photon lock-in detection with improved signal-to-noise ratio (which is described in detail elsewhere [27]).

III. SUPPRESSION OF ELECTRONIC FOUR-WAVE MIXING

The three-pulse scheme for SE-CARS allows different nonlinear contributions to be distinguished. Three distinct nonlinear processes can occur: two-pulse CARS ($\omega_{2\text{pCARS}}$), three-pulse trCARS (ω_{trCARS}), and FWM (ω_{FWM}) [Fig. 3(b)], with frequencies

$$\omega_{2\text{pCARS}} = \omega_p - \omega_S + \omega_p = \omega_p + \omega_v,$$

$$\omega_{\text{trCARS}} = \omega_p - \omega_S + \omega_x = \omega_x + \omega_v,$$

$$\omega_{\text{FWM}} = \omega_1 + \omega_2 - \omega_3,$$

assuming that the CARS process is on resonance, hence $\omega_v = \omega_p - \omega_S$. Any of the photons involved in CARS can also interact via nonresonant FWM such that $\omega_{1,2,3}$ can be equal to $\omega_{p,S,x}$. With degenerate pump and probe pulses used to perform trCARS ($\omega_p = \omega_x$), spectral separation of the two-pulse and trCARS signals is inherently impossible as $\omega_{2\text{pCARS}} = \omega_{\text{trCARS}}$. This adds a varying background in trCARS signals. Note that phase matching is not relevant for these experiments on single subwavelength-sized NPoMs.

To spectrally separate two-pulse and trCARS signals, the probe wavelength λ_x must be significantly detuned from the pump wavelength λ_p . While often achieved by frequency doubling of the pump or Stokes, this unfortunately directly

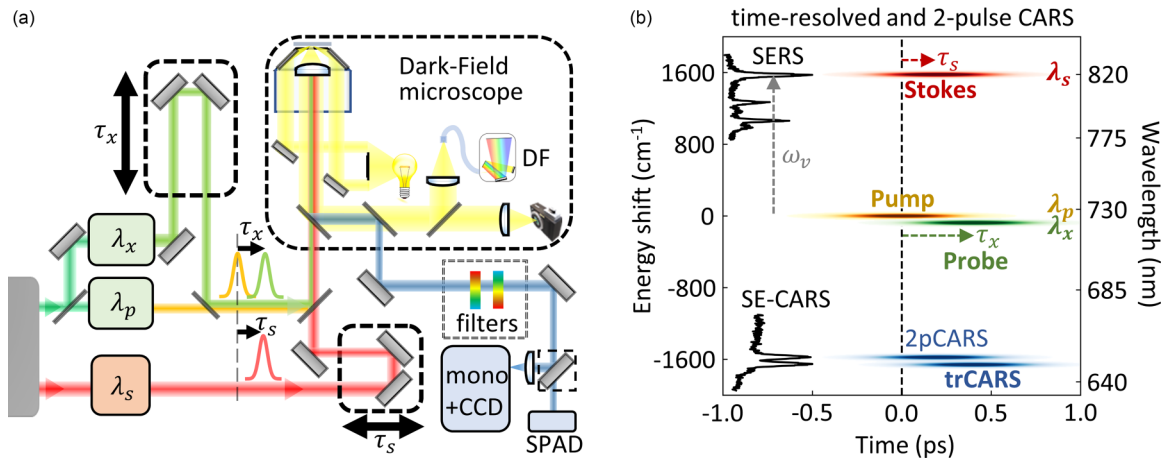


FIG. 2. Experimental setup. (a) Automated darkfield microscope combines three laser beams with variable time delay for SE-CARS. The signal is spectrally filtered and detected with a spectrometer (monochromator + CCD) or with a single-photon avalanche diode (SPAD) for single-photon lock-in detection. (b) Temporal-spectral pulse tunings for pump (p , yellow), Stokes (S , red), and probe (x , green), giving emission (blue) from two-pulse CARS (2pCARS) and three-pulse time-resolved CARS (trCARS). Top left, BPT SERS spectrum from pump only; bottom left, BPT SE-CARS spectrum from all three pulses.

pumps Au interband transitions, considerably increasing nanoscale damage. Other approaches using nonlinearly generated or electronically synchronized nondegenerate pulses reduce timing resolution (>1 ps), exceeding the phonon lifetime. The approach here retains spectral and temporal resolution by spectrally filtering the 10-nm-wide OPO output to

create two 1.5-nm pulses for the pump and probe beams. A similar approach has recently been employed for biological imaging using stimulated Raman scattering [38].

The three-color CARS scheme allows the BPT-filled NPoM to be driven at $\lambda_p = 726$ nm, $\lambda_s = 820$ nm, and $\lambda_x = 722$ nm, generating nonlinear emission spectra [Fig. 3(a), with $\tau_s = \tau_x = 0$ ps, average laser intensity $4 \mu\text{W} \mu\text{m}^{-2}$, and pulse energy 50 fJ]. Two strong peaks are observed at $\omega_{2p\text{CARS}} = 652$ nm and $\omega_{\text{trCARS}} = 649$ nm (slightly chirped). However, the third peak at $\omega_{\text{FWM}} = 646$ nm from FWM ($\omega_{\text{FWM}} = 2\omega_x - \omega_s$) is very weak. This FWM contribution is thus ten times smaller than the on-resonant CARS signals and may originate from off-resonant molecular CARS, electronic Raman scattering (ERS), or two-photon gold luminescence. We further confirm that the vibrationally resonant molecular CARS signal dominates over other FWM processes by scanning λ_p across the vibrational resonance. Only when the resonance condition $\omega_p - \omega_s = \omega_v$ is satisfied does a strong SE-CARS emission appear (see Fig. S2 of the Supplemental Material [36]).

These nonlinear experiments on BPT NPoMs demonstrate that the signal observed is dominated by molecular CARS. This is surprising in the context of many previous measurements that show FWM from metallic plasmonic components is very large [5,39–41]. The disparity arises from the different field distributions of different plasmonic architectures. The field E in NPoMs is tightly confined to the gap (of width d and permittivity ϵ_g) where the molecules reside, while field leakage into the metal (of permittivity ϵ_m) decays spatially within $\delta = d/2\epsilon_g \text{Re}\{1/\epsilon_m\} \sim 1$ nm [1]. Although both are enhanced by the plasmonic gap, the ratio of integrated SE-CARS to FWM given by the ratio of $|E|^8$ in the gap and in the metal is thus $2|\epsilon_m(\lambda_c)/\epsilon_g|^7 \sim 10^6$, much larger than in other plasmonic structures (for spherical Au nanoparticles this ratio is of order unity). This also explains observations of weaker FWM in closely spaced dimers [13]. Small-gap plasmonic structures hence generate large SE-CARS signals ($\sim 10^7$ counts/nJ³ here, still far below saturation) and

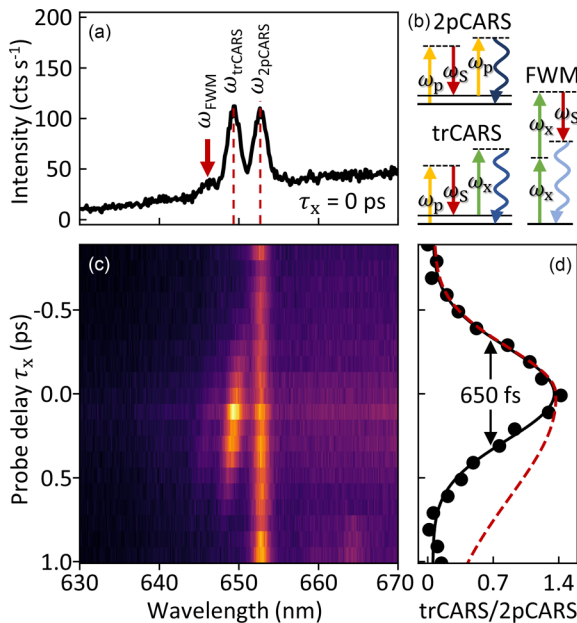


FIG. 3. SE-CARS spectrotemporal scan. (a) SE-CARS signal from BPT NPoM at 0 ps probe delay showing clear peaks at $\omega_{2p\text{CARS}}$ and ω_{trCARS} , but minimal peak at ω_{FWM} . (b) Excitation schemes for 2pCARS (pump-Stokes-pump), trCARS (pump-Stokes-probe), and FWM (probe-probe-Stokes). (c) Time-resolved SE-CARS spectra. (d) Integrated trCARS signal normalized by 2pCARS signal. Black line indicates Gaussian fit with 650 fs FWHM and red dashed line is the expected vibrational decay from CW SERS. Laser intensity $4 \mu\text{W} \mu\text{m}^{-2}$ per beam (pulse energy 50 fJ).

weak FWM in comparison to other plasmonic structures with $10\text{--}10^8$ -fold weaker SE-CARS [9,41,42].

IV. ACCELERATED MOLECULAR VIBRATIONAL DEPHASING

The clear evidence that trCARS signals originate from molecular vibrations allows us to explore their phonon dynamics. Scanning the time delay of the probe pulse, τ_x , allows a spectrotemporal map to be built [Fig. 3(c)]. Since the 2pCARS (at 652 nm) is independent of the probe pulse, no change is expected in its intensity. However, sporadic fluctuations are observed in time scans, most likely due to nanoscale modifications leading to changes in molecular coupling efficiency [32,33,43]. This simultaneous 2pCARS allows the trCARS signal (at 649 nm) to be normalized to reveal the true time-resolved intensity independent of transient signal fluctuations [Fig. 3(d)]. The extracted trCARS signal fits a Gaussian with FWHM of 650 fs corresponding to the convoluted excitation and probe pulses of 500 fs. The molecular dephasing time here is thus below the instrument response. In contrast, Fourier-transform analysis of cw SERS spectra [Fig. 1(d), red] suggests a molecular dephasing time of $T_2 > 600$ fs for this vibrational mode, indeed detectable with this setup [Fig. 3(d), red dashed curve]. This is faster than the original dephasing time in the absence of a nearby metal surface estimated as 2 ps in BPT powder, extracted from its Raman spectrum [Fig. 1(d), black]. More detail on Fourier analysis of Raman spectra to estimate CARS time tracks can be found in Fig. S3 of the Supplemental Material [36].

To explore the origin of accelerated dephasing times T_2 measured in trCARS, we investigate the phonon population lifetime T_1 with trIARS under similar laser intensities (see Appendix B). Here, the Stokes laser beam at ω_S is blocked and molecular vibrations are populated by spontaneous (incoherent) Stokes scattering of the pump or probe laser at $\omega_{p,x}$ [Fig. 1(b)]. This process has been termed “vibrational pumping” by the SERS community [44]. Since both the pump and probe pulses excite the vibration with equal laser intensity, an asymmetric decay is expected and observed in anti-Stokes scattering of both lasers, reversing for opposite time delays (see Appendix B Fig. 6). With an incoherent phonon population n_v excited by this process (see discussion in Appendix C), the extracted decay in n_v calculated from the anti-Stokes-to-Stokes ratio of the 1585 cm^{-1} vibrational mode measures the phonon population lifetime $T_1 = 600 \pm 300$ fs. This result demonstrates that trCARS and trIARS indeed probe different molecular properties and the accelerated coherence decay in trCARS is dominated by increased dephasing (instead of a higher phonon population decay rate).

The accelerated dephasing from trCARS implies that cw SERS and pulsed SE-CARS are probing the vibrational dephasing under different conditions. Critically, the peak powers of the pulsed lasers employed in SE-CARS are orders of magnitude higher than the cw average power, thereby driving the entire system (both vibrational states in molecules and metal as well as electronic and plasmonic states) out of thermal equilibrium [15]. Therefore, we reduce the pulsed laser intensity I_l by 20-fold to $200\text{ nW } \mu\text{m}^{-2}$ per beam (for pump, Stokes, and probe lasers; pulse energy 2.5 fJ), corre-

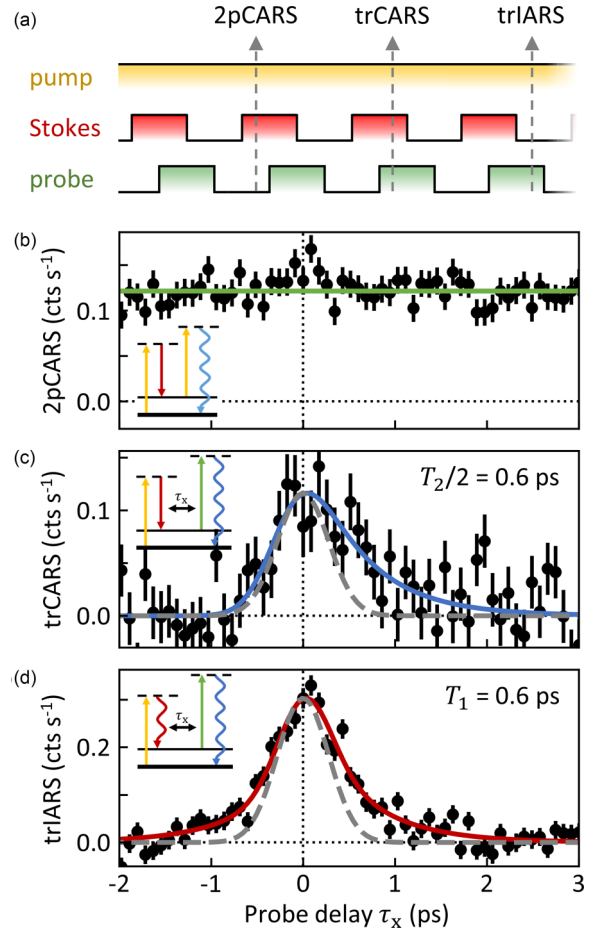


FIG. 4. Population and coherence decay from an individual NPoM. (a) Laser modulation scheme to identify different contributions to the signal with single-photon lock-in detection (50 kHz) [27]. (b) 2pCARS signal remains unchanged during probe delay scan. (c) trCARS signal of an individual NPoM shows one-sided decay with probe delay giving coherence lifetime T_2 . (d) trIARS signal decays on both sides of probe delay scan with population lifetime T_1 . Colored solid lines, exponential decay fit; grey dashed lines, instrument response from a pure FWM sample (without molecular layer). Laser intensity $200\text{ nW } \mu\text{m}^{-2}$ per beam (pulse energy 2.5 fJ). Error bars represent standard deviation of photon shot noise in each case.

sponding to peak fields in the nanogaps of order 10^8 V/m. We emphasize that these are used to excite transparent (non-electronically resonant) molecules, in contrast to other work using resonant dye molecules which damage far more rapidly. Since trCARS signals scale $\propto I_l^3$, recorded count rates are now almost four orders of magnitude lower and cannot be detected with a spectrometer and electron-multiplying charge coupled device (EMCCD) camera. Instead, we use single-photon avalanche detectors in combination with single-photon lock-in detection. Different nonlinear contributions to the signal count rate are distinguished by modulating Stokes and probe beams at 50 kHz [Fig. 4(a)] as described in detail previously [27]. Using this lock-in detection, we can simultaneously record time-delay scans of the 2pCARS, trCARS, and trIARS signals (which is not accessible with spectral analysis) on each individual NPoM. To acquire sufficient

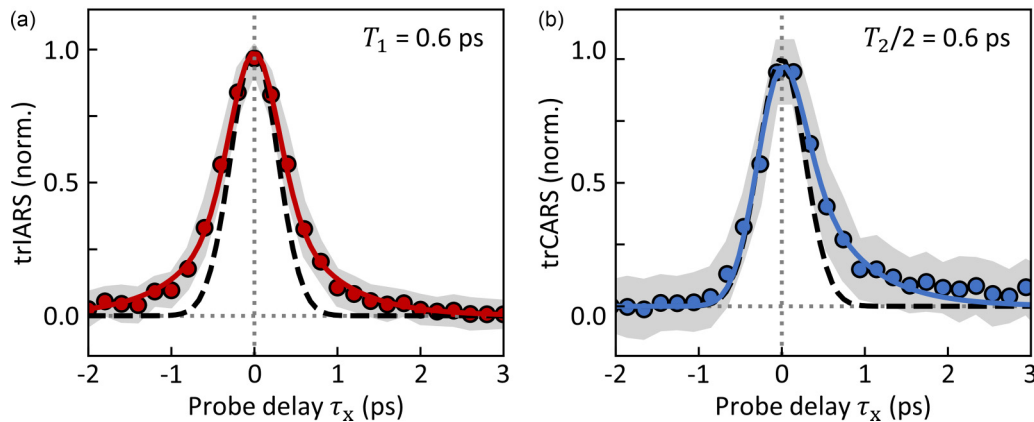


FIG. 5. Average population and coherence decay from many NPoMs. Single-photon (a) trIARS and (b) trCARS experiments from the selected 22 NPoMs showing a molecular response in trCARS. The average response is indicated by colored circles while the grey shaded area indicates the standard deviation of individual measurements. Colored lines are fits of the vibrational decay. The system response is indicated as a dashed black line. Raw data of all NPoMs is shown in Figure S6 of the Supplemental Material [36].

photon counts at these low powers, time tracks are integrated for 60 min. We emphasize that this is the lowest laser intensity used for CARS experiments so far reported [10], which prevents damage to the nanostructures and molecules (demonstrated by stable count rates during long integration times; see Supplemental Material Fig. S4 [36]). A spectrum of the light detected by the single-photon detector showing the different contributions to the count rate (2pCARS, trCARS, FWM, and ERS) is plotted in Fig. S5 of the Supplemental Material [36].

As expected, the 2pCARS signal is not modulated by sweeping the probe delay, showing the overall stability of the setup [Fig. 4(b)]. In contrast, both trCARS [Fig. 4(c)] and trIARS [Fig. 4(d)] signals vary with the time delay of the probe pulses. The model to fit these signals is described in detail in Appendix A. Since both pump and probe pulses can excite the vibration in trIARS and single-photon detection does not allow for spectral separation of the two components (as in Appendix B), the trIARS signal decays exponentially in both temporal directions [Fig. 4(d)]. Since the two-sided decay makes fitting the population lifetime difficult, the value obtained in Appendix B is used to fix $T_1 = 0.6$ ps. Figure 4(d) hence shows that the low-power trIARS measurement is consistent with the vibrational relaxation time measured at higher laser intensity. Therefore, we conclude that the rate of vibrational population relaxation is independent of pump power. The trCARS signal at low laser power here shows a decay slightly longer than the instrument response [grey dashed line in Fig. 4(c)] at positive probe pulse delay (probe pulses arriving after pump and Stokes). By fitting the trCARS data, the vibrational dephasing time can be extracted as $T_2/2 = 0.6$ ps = T_1 (the restriction $T_2 \geq 2T_1$ is applied to the fit; see Discussion below). However, the trCARS signal suffers from poorer signal-to-noise due to photon shot noise of the single-photon experiments. Here, a compromise is necessary between photon count rates and the lowest possible laser powers. Despite the higher noise, the low-power experiment here completely contrasts with data acquired at high power where only the system response is found (Fig. 3).

To increase confidence in these results, we carry out the experiment on more than 70 NPoM nanostructures. The trIARS and trCARS signal from each NPoM is normalized to the maximum of the fitted time track and shown in Fig. S6 of the Supplemental Material [36]. For trIARS measurements, the individual nanostructures consistently show a time-resolved response significantly longer than the system response. In contrast, trCARS time tracks are noisy and the molecular response cannot always be clearly distinguished from the system response. However, when individual trCARS measurements are examined, only $\sim 30\%$ of NPoMs show the molecular vibrational decay (one example is shown in Fig. 4) while other particles follow the system response. Hence, the trCARS signal of most NPoMs is dominated by the fast response of FWM and other backgrounds. In particular, the rapidly decaying broadband background from ERS cannot be distinguished from the trCARS signal in single-photon experiments (spectral selection is not possible in this setup).

We therefore select the 22 NPoMs clearly showing the molecular response in trCARS to analyze the vibrational dynamics in low-power experiments. The average trIARS time track of these 22 NPoMs fits well a molecular relaxation with $T_1 = 0.6$ ps, as observed before [Fig. 5(a)]. In trCARS, the molecular dephasing is consistent across all particles showing the molecular response, with the standard deviation of individual measurements well distinguished from the system response [Fig. 5(b)]. Fitting the vibrational dephasing again yields $T_2/2 = 0.6$ ps = T_1 . Therefore, we conclude that dephasing occurs on similar characteristic timescales in all NPoMs when the molecular signal can be distinguished from backgrounds. In comparison to high-power experiments, single-photon measurements at minimally small laser powers thus show that vibrational dephasing is modified in NPoMs by processes depending on excitation intensity. While the vibrational relaxation time T_1 is independent of laser power, vibrational dephasing with T_2 is accelerated at high powers, implying power-dependent dephasing processes in NPoMs. Potential physical processes leading to this effect are discussed below. For a more detailed analysis of time tracks from individual NPoMs see Appendix D.

V. DISCUSSION

We now compare the results obtained from different experimental settings. For trIARS experiments, both high- and low-power measurements agree, giving $T_1 = 0.6$ ps. Therefore, the vibrational relaxation of BPT in the plasmonic nanocavity seems unaffected by decay processes depending on laser power. In contrast, different results are obtained for dephasing times from different experiments. While trCARS at low laser power measures $T_2/2 = 0.6$ ps, high-power trCARS is unable to probe the vibrational decay and instead just retrieves the system response. Consistent with low-power experiments, the linewidth of cw SERS spectra also suggests dephasing times of $T_2/2 = 0.6$ ps. Moreover, vibrational population relaxation and dephasing are not independent measurements. In the Markovian approximation (no inhomogeneous broadening), the vibrational dephasing time T_2 is linked to the population lifetime T_1 via the pure dephasing time T_2^* through [28]

$$\frac{1}{T_2} = \frac{1}{2T_1} + \frac{1}{T_2^*}.$$

Hence, both vibrational relaxation and pure dephasing processes contribute to the dephasing time T_2 experimentally measured with trCARS. In general, any vibrational coherence induced in the sample cannot last longer than the lifetime of the vibrational population, thus limiting $T_2 \leq 2T_1$. In low-power measurements carried out here (both cw SERS and single-photon trCARS), we observe $T_2 = 2T_1$, indicating that pure dephasing processes are slow compared to the vibrational relaxation. However, increasing the laser power accelerates the dephasing while vibrational relaxation remains constant. Therefore, pure dephasing processes depending on excitation power must be present for molecules in the NPoM nanocavity.

We now discuss physical processes that could lead to accelerated dephasing under high excitation intensity. As demonstrated in Fig. S7 of the Supplemental Material [36], illuminating the NPoM structures with laser pulses strongly drives the system out of thermal equilibrium with temperatures extracted from different vibrational modes varying drastically. While molecular vibrations are populated by vibrational pumping [44], electronic excitations (“hot electrons”) are directly induced by the laser pulses followed by fast thermalization of electronic states [45]. Therefore, trCARS probes the dephasing of molecular vibrations for a system in its nonequilibrium state, with effective temperature (representing vibrational and electronic populations) transiently increased far above room temperature.

Excitation-induced dephasing (EID) is well known for excitonic systems, such as semiconductors [46] or carbon nanotubes [47]. In EID, electronic excited-state interactions (such as excitonic screening) accelerate dephasing depending on the concentration of excited carriers, which typically scales linearly with pump laser power [47]. Electronic excitations can, however, also induce dephasing of vibrational states via electron-phonon interactions. In graphene, hot carriers induced by ultrafast laser pulses can increase vibrational dephasing by electron-phonon scattering, leading to a laser-power-dependent broadening of Raman lines [48]. Since

molecular vibrations and metal are separated in our NPoM experiments, a corresponding model would involve excitation of hot electrons in the metal which then interact with vibrations of molecules bound to the metal. For Cs atoms adsorbed to a Pt surface, a fast vibrational dephasing process depending on laser intensity was observed, attributed to scattering of hot electrons at the adsorbate [49]. A similar mechanism could explain power-dependent dephasing in our experiments; however, further theory is required.

In addition to electron-phonon scattering, phonon-phonon interactions could also be a source of vibrational dephasing. A previously postulated explanation for increasing vibrational dephasing is the vibrational energy exchange (VEE) model [50–52]. Here, the vibrational mode under investigation couples to another vibrational exchange mode, resetting the vibrational phase via scattering to the coupled mode and back. This interaction importantly depends on the population in the exchange mode, thus increasing here as (all) vibrational modes are transiently populated by laser pulses. Previously, the VEE model has only been employed to explain the temperature-dependent Raman linewidth at cryogenic temperatures, and coupling to lower-energy vibrations was found [51,52]. Here, the system is transiently excited by laser pulses, opening up the possibility of VEE with higher-energy vibrations. While the signal-to-noise ratio of our data is insufficient to prove unambiguously that the effects observed here are caused by a VEE-type model, we provide a detailed analysis of the experimental data in the context of a VEE model in Appendix D.

Another possible explanation for increased dephasing under strong driving is vibrational anharmonicity, which slightly shifts vibrational frequencies leading to phase drift. However, there is no evidence for such frequency shifts in SERS spectra at higher laser power (see Fig. S7 of the Supplemental Material [36]). Other mechanisms that lead to an accelerated phonon decay, such as electron friction from the bond to the metal surface, have been discussed in the literature but should not depend on excitation intensity [53].

This observation that vibrational dephasing of molecules is enhanced under strong excitation is relevant for understanding many complex molecular phenomena, in particular on substrates providing high plasmonic surface enhancement. These include metal contact effects in molecular electronics, catalysis of chemical reactions at metal surfaces, heat transfer from molecules at metals for organic thermoelectrics, and other situations where the coupling of vibrational modes to electronic and energy transport is relevant.

VI. CONCLUSIONS

In summary, we demonstrate how two-pulse and three-pulse optical nonlinearities resonant with molecular vibrations are strongly enhanced by plasmonic nanocavities. In the NPoM geometry, molecular CARS signals dominate over FWM as well as all electronic Raman contributions. Since the dephasing time is very sensitive to the driving laser intensity, ultralow excitation powers are required to investigate vibrational decays. Using single-photon lock-in

detection, we simultaneously explore vibrational population decay and dephasing in BPT and show that pure dephasing is accelerated by excitation-power-dependent processes in the NPoM nanocavity. These ultrafast spectroscopy experiments on ~ 100 molecules pave the way towards exploring single-molecule dynamics under ambient conditions and demonstrate an optical probe for modified molecular dynamics under extreme optical field confinement.

Data for all figures can be found at Ref. [54].

ACKNOWLEDGMENTS

We thank Ruben Esteban for fruitful discussions. We acknowledge support from European Research Council (ERC) under Horizon 2020 research and innovation programme THOR (Grant Agreement No. 829067), PICOFORCE (Grant Agreement No. 883703), and UK EPSRC Grants No. EP/L027151/1 and No. EP/R020965/1. L.A.J. acknowledges support from the Cambridge Commonwealth, European & International Trust and EPSRC Award No. 2275079. R.A. acknowledges support from the Rutherford Foundation of the Royal Society Te Apārangi of New Zealand, the Winton Programme for the Physics of Sustainability, and Trinity College, University of Cambridge. B.d.N. acknowledges support from Winton Programme for the Physics of Sustainability and the Royal Society (Grant No. URF/R1\211162). N.S.M. acknowledges support from the German National Academy of Sciences Leopoldina.

L.A.J., W.M.D., and J.J.B. devised the experimental techniques and developed data analysis and theory. R.A., B.d.N. and N.S.M. fabricated samples. All authors contributed to writing the manuscript.

The authors declare no conflicts of interest.

APPENDIX A: EXPERIMENTAL METHODS

1. Sample preparation

Template-stripped gold substrates were prepared by thermal evaporation of 100 nm of gold on silicon, with glass substrates glued with UV glue Norland 81 (Thorlabs), UV cured, and a fresh sample stripped off for each use. Self-assembled monolayers (SAMs) of biphenyl-4-thiol (BPT) were fabricated by soaking a template-stripped gold substrate in 1 mM BPT (Sigma-Aldrich) solution in 200-proof anhydrous ethanol overnight. After SAM formation, the sample was cleaned with ethanol and blown dry with nitrogen. Nanoparticle-on-mirror samples were prepared by depositing 50 μL of 80-nm gold nanoparticles (AuNPs, BBI Solutions) on BPT SAMs on template-stripped gold, which were then rinsed off with deionized water after 30 s and blown dry with nitrogen. Polymer-coated NPoM samples were prepared by spin-coating a 100-nm layer of PMMA (950k molecular weight, 2 wt% in anisole) with a first cycle at 500 rpm for 10 s, then a second at 2000 rpm for 45 s. Samples were then left to bake on a hotplate at 50 $^{\circ}\text{C}$ for 5 min to remove residual anisole solvent.

2. CARS

A Spectra-Physics MaiTai pump laser (80 MHz, 100 fs) drives an optical parametric oscillator (Spectra-Physics In-

spire) to generate three pulse trains of different wavelengths. These are filtered by independently tunable bandpass filters (PhotonETC LLTF contrast) with a spectral bandwidth of 1.5 nm and temporal width of 0.5 ps. Laser pulses are temporally aligned with motorized delay stages. Two of the three laser beams are modulated at 50 kHz with electro-optical modulators for lock-in detection.

NPoMs are located with an Olympus 0.9 NA, 100 \times dark-field objective in a custom-built, automated microscope. Laser pulses are focused on the sample and signal is collected in reflection by the same objective. Tunable edgepass filters (Fianium Superchrome) remove the laser pulses and other background. Spectra are recorded with an Andor iDus CCD camera (DU416A) on an Andor Shamrock monochromator (SR-303i-B). Alternatively, a single-photon avalanche diode from Micro Photon Devices (SPD-100-CTD) was used to detect the signal.

Single-photon multiclock lock-in detection was realized by recording arrival timestamps of all photons at the detector along with timestamps from several reference signals (80 MHz laser repetition rate, 50 kHz laser modulation, 1 Hz delay stage sweep). Photon timestamping with picosecond accuracy was achieved using a field-programmable gate array board (Digilent Arty Z7) and specially designed software. Extracting the relative phase of the photon arrival compared to each reference signal allows to measure the periodic modulation of the signal during the reference period in time. This technique is described in more detail elsewhere [27].

3. Fitting of trCARS and trIARS single-photon time tracks

The vibrational response in single-photon experiments is extracted by exponential decay fits to the measured time tracks. For the trIARS signal, three components have to be accounted for: (i) the pump-probe and (ii) probe-pump process each lead to an exponential decay (towards opposite temporal directions) convoluted with the system response (Gaussian of FWHM 650 fs). Since laser intensities can vary slightly, the intensity of these two signals is fitted individually. Additionally, (iii) the fast ERS response [which cannot be separated spectrally in single-photon experiments but is visible in Fig. 6(d)] gives a quickly decaying contribution which is included in the fit with a Gaussian corresponding to the system response at $t = 0$. In single-photon experiments, the two-sided exponential decay leads to a large error in the extraction of T_1 . Hence, the vibrational relaxation is taken from Appendix B using high-power experiments that yield $T_1 = 0.6$ ps (see Fig. 6). For trCARS, two processes contribute to the signal. The molecular vibrational response is fitted by an exponential decay convoluted with the system response (only towards positive time delays here). In addition, the nonresonant FWM and other background signals (such as electronic Raman scattering) are accounted for by a Gaussian at $t = 0$ with the width of the system response (see Fig. S5 of the Supplemental Material [36] for a spectral analysis). The restriction $T_2 \leq 2T_1$ is applied to the fit, again with $T_1 = 0.6$ ps, to avoid unphysical dephasing times.

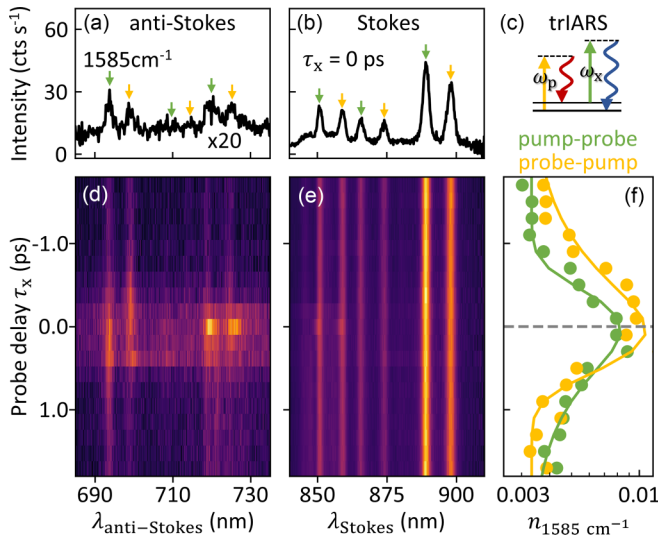


FIG. 6. trIARS spectrotemporal scan. (a) Anti-Stokes and (b) Stokes spectra of BPT NPoM at 0 ps probe delay showing two sets of SERS peaks from three vibrational modes, corresponding to scattering by the pump ($\lambda_p = 787$ nm, yellow arrows) and probe ($\lambda_x = 779$ nm, green arrows). (c) Excitation scheme for trIARS. (d) Anti-Stokes and (e) Stokes trIARS spectra with changing probe time delay. (f) Phonon population of the 1585 cm^{-1} vibrational mode extracted from the Stokes/anti-Stokes ratio. Both the pump-probe (green) and probe-pump (yellow) process can excite the vibration. An exponential decay fit (lines) of both time tracks yields $T_1 \approx 600$ fs. Laser intensity $1 \mu\text{W} \mu\text{m}^{-2}$ per beam (pulse energy 12.5 fJ).

APPENDIX B: trIARS SPECTROTEMPORAL SCAN

Time-resolved incoherent Raman scattering (trIARS) experiments are carried out with two laser beams which have a photon energy difference that does not match the energy of any vibration (pump, $\lambda_p = 787$ nm; probe, $\lambda_x = 779$ nm). The laser pulses are prepared by sending the pump laser (tuned to 780 nm) through a short single-mode fiber (for spectral broadening of 50 nm), and subsequent filtering by tunable bandpass filters. Both lasers are attenuated to $1 \mu\text{W} \mu\text{m}^{-2}$ average intensity (pulse energy 12.5 fJ) on the sample. Full SERS spectra are acquired by removing the laser scatter with 785 -nm notch filters.

In the recorded spectra, two sets of SERS peaks are visible, originating from scattering of the pump or probe pulses [Figs. 6(a) and 6(b)]. Scanning the time delay of the probe pulses leaves the Stokes spectrum unchanged [Fig. 6(e)]. The anti-Stokes spectrum, on the other hand, shows increased signal when both pulses overlap in time, with an increase in SERS peaks from molecular vibrations as well as an increase of the broadband ERS background originating from hot electrons pumped by the laser pulses. Here, we focus our analysis on the peak area of the vibrational mode investigated with trCARS in Fig. 3 at 1585 cm^{-1} .

From the ratio of Stokes (S_S) to anti-Stokes (S_{aS}) scattering, the phonon population n_v of the corresponding vibrational

mode can be extracted using

$$n_v = \frac{\omega_S^4}{\omega_{aS}^4} \left(\frac{S_S}{S_{aS}} - \frac{\omega_S^4}{\omega_{aS}^4} \right)^{-1}$$

with the frequency of Stokes and anti-Stokes photons ω_S and ω_{aS} , respectively. Furthermore, the phonon population can also be expressed as the temperature at which a vibration of energy $\hbar\omega_v$ would reach this population by thermal excitation. However, since the vibrations are strongly excited by vibrational pumping from ultrafast excitation, the measured phonon populations are not thermalized and the extracted temperatures will vary strongly between modes (see Fig. S7 of the Supplemental Material [36]). In Fig. 6(f), the phonon population with changing probe delay is calculated for both the pump-probe and probe-pump processes for the 1585 cm^{-1} vibration. Both time tracks show an exponential decay, but to opposing temporal ordering since in one process the "pump" pulses act as the excitation source while in the other it is the "probe" pulses which are the excitation. Exponential fits of these two measurements result in similar vibrational lifetimes of $T_1 = 600 \pm 300$ fs. This result is consistent with low-power measurements carried out in Figs. 4 and 5.

APPENDIX C: COHERENCE IN SERS VIBRATIONAL PUMPING

Most time-resolved Raman experiments to study molecular vibrational dynamics use the coherent Raman techniques CARS or stimulated Raman scattering (SRS). As coherent techniques, these methods probe the decay of vibrational coherence in the material, thus measuring the dephasing lifetime T_2 . In the first experiments to instead investigate the decay of the vibrational population T_1 , vibrations were excited coherently by SRS and spontaneous anti-Stokes scattering was separated from CARS by a detection angle outside the phase-matching condition [55,56]. Since the experiments in our work are carried out in sub-wavelength-sized hotspots, trCARS and trIARS here cannot be distinguished by the angle of detection. A different approach to measure T_1 is to generate an incoherent phonon population by excitation and subsequent incoherent decay of electron-hole pairs [57,58], as is well established for trIARS studies of carbon nanomaterials [23–26]. In these experiments (often conducted under focused laser excitation conditions), it is not necessary to separate coherent and incoherent contributions through the detection angle since the laser pulse energy differences are not tuned resonantly to the molecular vibrations and the SRS process is hence not possible. Here, we similarly excite an incoherent phonon population for trIARS but avoid direct electronic excitation. Instead, the strong surface-enhanced optical fields in plasmonic nanocavities enable direct vibrational pumping of the molecules by increasing spontaneous Stokes scattering rates (while keeping laser photon energies far below the band gap of any electronic excited states).

To understand whether the phonon population produced in vibrational pumping by spontaneous Stokes scattering is coherent, we compare this process to spontaneous parametric down-conversion of a pump photon (Fig. 7). In this nonlinear process, one photon of the pump laser at ω_p is converted into

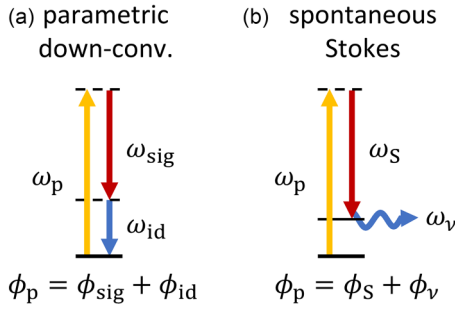


FIG. 7. Comparison of spontaneous nonlinear processes. (a) Excitation scheme of spontaneous parametric down-conversion involving three photons. (b) Excitation scheme of spontaneous Stokes scattering involving two photons (straight arrows) and one phonon (curved arrow). The phase of the phonon, ϕ_v , is random if the Stokes photon is generated spontaneously.

two photons of lower energy (signal at ω_{sig} and idler at ω_{id}) under conservation of energy and momentum. The phase of the outgoing photons is connected to the phase of the pump photon via $\phi_p = \phi_{sig} + \phi_{id}$ [59]. Similarly, in spontaneous Stokes scattering the phase of the Stokes photon, ϕ_S , and the phase of the generated vibration, ϕ_v , obey $\phi_p = \phi_S + \phi_v$. Hence, the molecular vibrations are generated with random phase by vibrational pumping if the process is not stimulated by laser pulses at the Stokes frequency (which fixes ϕ_S with respect to ϕ_p). In our experiment, the plasmonic nanocavities form a very lossy optical cavity (Q factor ~ 10 [31]), so light in the cavity decays fully between laser pulses, and Stokes signal emission rates (~ 1 kHz) are much lower than the laser repetition rate (80 MHz) and scale linearly with laser intensity (see Fig. S7(d) of the Supplemental Material [36]). Therefore, the system is far below the SRS threshold and phonons will be generated with random phase. The resulting phonon population n_v is thus incoherent, and its decay probes the phonon lifetime T_1 .

Recent reports have demonstrated that a monolayer of molecules inside the NPoM nanocavity can exhibit collective vibrations of hundreds of molecules [35,60,61]. This implies coherence between vibrations of different molecules even under spontaneous Raman scattering conditions. However, this does not contradict the above discussion since the pump photons scatter directly with the bright collective phonon mode in this optomechanical system and populate this new collective mode directly. In the optomechanical description, this can be shown by a transformation of the equations to a set of collective phonon operators which leads to identical results as treating all molecules individually [60]. While components of the vibration in individual molecules are coherent to each other, different phonons in the collective mode are still generated with random phase by spontaneous Stokes scattering and hence give an incoherent (collective) phonon population from which incoherent anti-Stokes scattering is observed in our trIARS experiment.

APPENDIX D: VIBRATIONAL ENERGY EXCHANGE

The vibrational energy exchange (VEE) model [50] describes this interaction of different phonon populations and

proposes an increase of the dephasing rate Γ_2 as

$$\Gamma_2 = \Gamma_2^0 + A \exp \left\{ -\frac{\hbar\omega_e}{k_B T_{ne}} \right\},$$

where Γ_2^0 is the original dephasing rate and A combines multiple parameters of the VEE model which cannot be disentangled with our setup. We note that previously the VEE model has only been employed to explain the temperature-dependent Raman linewidth at cryogenic temperatures, and coupling to lower-energy vibrations was found [51]. Here, we apply the model to a system transiently driven far above room temperature by laser pulses which is thus more sensitive to exchange with higher-energy vibrations.

To analyze our results quantitatively in the context of the VEE model, we fit trCARS and trIARS time tracks of 40 individual NPoMs to extract the experimentally measured vibrational decay parameters. Since this analysis suffers from large uncertainties in the measurement of vibrational dephasing times due to the poor experimental signal-to-noise ratio [SNR; see Fig. 4(c)], the results presented in this appendix cannot provide unambiguous proof that the effect observed is caused by VEE, but are a helpful comparison. Figure 8(a) shows the range of parameters extracted from probe delay scans on individual NPoMs. The dephasing rate $\Gamma_2 = 1/T_2$ varies considerably between NPoM structures while the population decay rate $\Gamma_1 = 1/T_1$ shows a much narrower distribution. To understand the origin of these deviations, we plot the decay rates against the maximum signal count rate at $\tau_x = 0$ ps [Figs. 8(c) and 8(d)]. A clear positive correlation between signal count rates and dephasing rates is observed for trCARS. Particles with higher signal count rates show systematically faster dephasing while population decay rates from trIARS remain constant. The mean vibrational population lifetime T_1 of 420 ± 110 fs is similar to values extracted in the main text with more robust analysis of averaged time tracks. Other potential parameter correlations have been investigated (see Fig. S8 of the Supplemental Material [36]), but no correlations are found. We note that this analysis of decay parameters finds $\Gamma_2 < \Gamma_1$ for some NPoMs which must be unphysical and may be caused by the low SNR in trCARS time tracks of individual particles.

Signal count rates vary strongly between NPoMs due to different light in- and outcoupling efficiencies governed by nanoparticle polydispersity and differences in contact facet size and shape [62,63]. Hence, the acquired signal count rate is closely connected to the laser intensity coupled into the gap and we can calculate the incoupling efficiency η_i for every NPoM i as $\eta_i = S_i/\text{mean}(S_i)$ from each particle with signal count rate S_i . Using this efficiency, we can estimate the incoupled laser intensity experienced by the NPoM in Figs. 8(e) and 8(f) as $I_i^{\text{in}} = \sqrt[3]{\eta_i} I_l$ (where the cubic root arises from $S_{\text{CARS}} \propto I_l^3$) [35]. Accordingly, higher signal count rates correspond to a higher laser intensity experienced by the system. While the population decay rate is independent of laser intensity [Fig. 8(e)], the coherence decay rate scales with $\Gamma_2 \propto I_l^2$ [Fig. 8(f)]. This is consistent with high-power experiments giving a strongly accelerated dephasing below the instrument response [Fig. 3(d)].

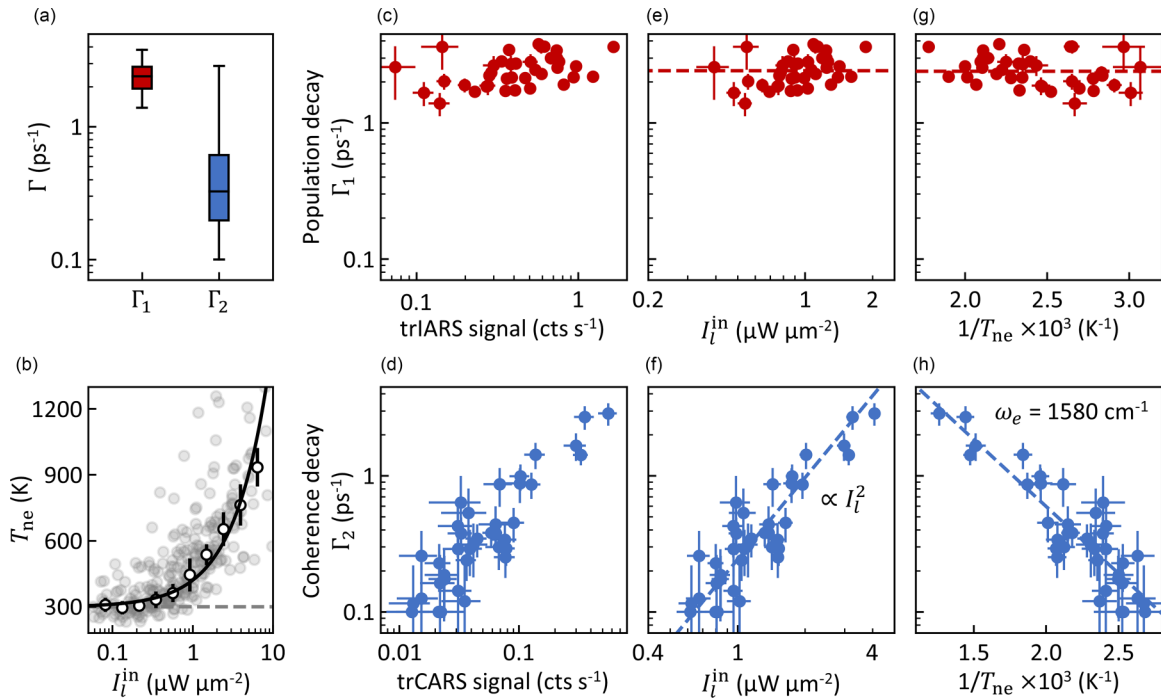


FIG. 8. Decay parameter analysis for many NPoMs. (a) Boxplots showing range of values for population decay Γ_1 (red) and coherence decay Γ_2 (blue) from 40 NPoMs. (b) Nonequilibrium temperature T_{ne} extracted from electronic anti-Stokes scattering vs incoupled average laser intensity I_l^{in} (at 785 nm) for 30 NPoMs. Fit to $T_{ne} = 300 \text{ K} + a \cdot I_l^{in}$ (solid black line, a : fit parameter) giving temperature calibration for (g) and (h). Correlation of decay rates with amplitude of detected signal for (c) Γ_1 and (d) Γ_2 for 40 NPoMs. For the coherence decay, a stronger signal is correlated with a faster decay. Decay rates with increasing total incoupled laser intensity: (e) population decay rates remain constant (red dotted line) while (f) dephasing rates increase quadratically with intensity (blue dotted line). Decay rates vs inverse temperature for (g) Γ_1 with constant mean (red dotted line) and (h) Γ_2 with fit of VEE model (blue dotted line). From the fit, the energy of the exchange mode ω_e can be determined. Error bars in (c)–(h) show a standard error of fit parameters.

We confirm this observation by sweeping the laser power on one NPoM while recording trCARS and trIARS (see Fig. S9 of the Supplemental Material [36]). We find again that the population decay is independent of the incident laser intensity while the dephasing rate scales quadratically with intensity. This observation agrees well with the data in Fig. 8 recorded on many NPoMs.

Illuminating the NPoM with laser pulses strongly drives the system out of thermal equilibrium, as investigated with power-dependent SERS spectra in Fig. S7 of the Supplemental Material [36]. Since vibrational pumping directly excites phonons via surface-enhanced Stokes scattering [44], Stokes-to-anti-Stokes ratios of different vibrational modes can lead to apparent temperatures varying drastically between modes. These apparent temperatures directly represent the (driven) phonon population of each mode, rather than the (equilibrium) temperature of the full system. Furthermore, the low-wavenumber background from ERS gives information about the temperature of thermalized electrons in the surrounding metal facets. After excitation of "hot" electrons, thermalization on timescales $< 100 \text{ fs}$ by electron-electron scattering to a Boltzmann distribution occurs [45], which is fit in Fig. S7 [36] to obtain the nonequilibrium temperature T_{ne} of the nanostructure at the pulse peak [64]. While the ERS background provides the fastest relaxation to a thermalized population in the system, it still does not represent

the nonequilibrium temperature of other molecular phonon modes.

Analyzing the temperature of the thermalized ERS background reveals that the peak temperature increases with incoupled laser intensity, reaching apparent nonequilibrium temperatures up to 1000 K above room temperature at $10 \mu\text{W} \mu\text{m}^{-2}$ [Fig. 8(b)]. This compares to $< 1 \text{ K}$ increases at typical cw laser powers used in SERS (at higher average powers). Therefore, SE-CARS experiments even at the lowest pulsed laser intensities probe the vibrational dynamics of a system transiently driven strongly out of thermal equilibrium by the laser pulses with the effective temperature highly dependent on each individual NPoM incoupling efficiency. We thus use this ERS temperature to calibrate incoupled laser intensities obtained in trCARS experiments to estimate NPoM nonequilibrium temperatures during each experiment [black line in Fig. 8(d)]. However, calibrating the temperature of the entire NPoM system with the electronic temperature (which is not equivalent to the vibrational temperatures in this nonequilibrium system) adds uncertainty to the analysis here.

We observe $\ln(\Gamma_2) \propto 1/T_{ne}$ for the coherence decay Γ_2 , while the population decay Γ_1 is independent of T_{ne} [Figs. 8(g) and 8(h)]. One previously postulated explanation for accelerated dephasing at increasing temperature is coupling of the resonantly excited phonon mode (ω_v) to another vibrational

exchange mode at ω_e populated by the transient increase in temperature T_{ne} [51,52].

Fitting the VEE model to the data allows us to estimate the energy of the exchange mode ω_e and thereby study the mechanism of dephasing. For the dephasing rate Γ_2 we find $\omega_e = 1580 \pm 140 \text{ cm}^{-1}$, suggesting that dephasing is dominated by scattering with phonons of the resonantly pumped mode ω_v itself. Investigations of a different molecule (triphenyl-4-thiol) and vibrational mode (1080 cm^{-1} of BPT) (Supplemental Material Fig. S10 [36]) confirm that, within the margin of error of this model, dephasing is driven by self-interactions of the pumped vibration. This intriguing result implies that fluctuations in the density of vibrations of this harmonic oscillator lead to nonlinear phase drift, potentially through

anharmonicity of the vibrational potential. By contrast, the vibrational population decay can be more than tenfold faster than the dephasing and is not depending on T_{ne} , suggesting a different decay mechanism.

Dephasing mediated by energy exchange with the increased population in the vibration excited resonantly is consistent with the quadratic dependence of Γ_2 on laser intensity observed above (see Fig. 8(f), and Fig. S9 of the Supplemental Material [36]). Since the phonon population n_v of the resonant vibration at ω_v is driven in CARS with $n_v \propto I_l^2$, the observation of $\Gamma_2 \propto I_l^2 \propto n_v$ is equivalent to the VEE model resulting in an exchange mode $\omega_e = \omega_v$. Hence, we conclude that the temperature extracted from the ERS background here is a valid representation of the driven NPoM system.

-
- [1] J. J. Baumberg, J. Aizpurua, M. H. Mikkelsen, and D. R. Smith, Extreme nanophotonics from ultrathin metallic gaps, *Nat. Mater.* **18**, 668 (2019).
- [2] A. B. Taylor and P. Zijlstra, Single-molecule plasmon sensing: Current status and future prospects, *ACS Sensors* **2**, 1103 (2017).
- [3] P. Lalanne, S. Coudert, G. Duchateau, S. Dilhaire, and K. Vynck, Structural slow waves: Parallels between photonic crystals and plasmonic waveguides, *ACS Photon.* **6**, 4 (2019).
- [4] N. C. Lindquist, C. D. L. de Albuquerque, R. G. Sobral-Filho, I. Paci, and A. G. Brolo, High-speed imaging of surface-enhanced Raman scattering fluctuations from individual nanoparticles, *Nat. Nanotechnol.* **14**, 981 (2019).
- [5] K. T. Crampton, A. Zeytunyan, A. S. Fast, F. T. Ladani, A. Alfonso-Garcia, M. Banik, S. Yampolsky, D. A. Fishman, E. O. Potma, and V. A. Apkarian, Ultrafast coherent Raman scattering at plasmonic nanojunctions, *J. Phys. Chem. C* **120**, 20943 (2016).
- [6] N. L. Gruenke, M. F. Cardinal, M. O. McAnally, R. R. Frontiera, G. C. Schatz, and R. P. Van Duyne, Ultrafast and nonlinear surface-enhanced Raman spectroscopy, *Chem. Soc. Rev.* **45**, 2263 (2016).
- [7] S. Yampolsky, D. A. Fishman, S. Dey, E. Hulkko, M. Banik, E. O. Potma, and V. A. Apkarian, Seeing a single molecule vibrate through time-resolved coherent anti-Stokes Raman scattering, *Nat. Photon.* **8**, 650 (2014).
- [8] C. Steuwe, C. F. Kaminski, J. J. Baumberg, and S. Mahajan, Surface enhanced coherent anti-Stokes Raman scattering on nanostructured gold surfaces, *Nano Lett.* **11**, 5339 (2011).
- [9] T. Ichimura, N. Hayazawa, M. Hashimoto, Y. Inouye, and S. Kawata, Tip-enhanced coherent anti-Stokes Raman scattering for vibrational nanoimaging, *Phys. Rev. Lett.* **92**, 220801 (2004).
- [10] S. Abedin, K. Roy, X. Jin, H. Xia, S. R. J. Brueck, and E. O. Potma, Surface-enhanced coherent anti-Stokes Raman scattering of molecules near metal-dielectric nanojunctions, *J. Phys. Chem. C* **126**, 8760 (2022).
- [11] E. L. Keller and R. R. Frontiera, Ultrafast nanoscale Raman thermometry proves heating is not a primary mechanism for plasmon-driven photocatalysis, *ACS Nano* **12**, 5848 (2018).
- [12] Z. Yu and R. R. Frontiera, Intermolecular forces dictate vibrational energy transfer in plasmonic-molecule systems, *ACS Nano* **16**, 847 (2022).
- [13] Y. Zhang, Y.-R. R. Zhen, O. Neumann, J. K. Day, P. Nordlander, and N. J. Halas, Coherent anti-Stokes Raman scattering with single-molecule sensitivity using a plasmonic Fano resonance, *Nat. Commun.* **5**, 4424 (2014).
- [14] J. M. Klingsporn, M. D. Sonntag, T. Seideman, and R. P. Van Duyne, Tip-enhanced Raman spectroscopy with picosecond pulses, *J. Phys. Chem. Lett.* **5**, 106 (2014).
- [15] A. Lombardi, M. K. Schmidt, L. Weller, W. M. Deacon, F. Benz, B. de Nijs, J. Aizpurua, and J. J. Baumberg, Pulsed molecular optomechanics in plasmonic nanocavities: From nonlinear vibrational instabilities to bond-breaking, *Phys. Rev. X* **8**, 011016 (2018).
- [16] R. E. Littleford, D. Cunningham, P. Matousek, M. Towrie, A. W. Parker, I. Khan, D. McComb, and W. E. Smith, Surface-enhanced resonance Raman scattering using pulsed and continuous-wave laser excitation, *J. Raman Spectrosc.* **36**, 600 (2005).
- [17] E. A. Pozzi, N. L. Gruenke, N. Chiang, D. V. Zhdanov, N. Jiang, T. Seideman, G. C. Schatz, M. C. Hersam, and R. P. Van Duyne, Operational regimes in picosecond and femtosecond pulse-excited ultrahigh vacuum SERS, *J. Phys. Chem. Lett.* **7**, 2971 (2016).
- [18] Q. Lin, S. Hu, T. Földes, J. Huang, D. Wright, J. Griffiths, B. de Nijs, E. Rosta, and J. J. Baumberg, Optical suppression of energy barriers in single molecule-metal binding, *Sci. Adv.* **8**, eabp9285 (2022).
- [19] J.-X. Cheng, L. D. Book, and X. S. Xie, Polarization coherent anti-Stokes Raman scattering microscopy, *Opt. Lett.* **26**, 1341 (2001).
- [20] F. Ganikhanov, C. L. Evans, B. G. Saar, and X. S. Xie, High-sensitivity vibrational imaging with frequency modulation coherent anti-Stokes Raman scattering (FM CARS) microscopy, *Opt. Lett.* **31**, 1872 (2006).
- [21] J. X. Cheng, A. Volkmer, L. D. Book, and X. S. Xie, Epi-detected coherent anti-Stokes Raman scattering (E-CARS) microscope with high spectral resolution and high sensitivity, *J. Phys. Chem. B* **105**, 1277 (2001).
- [22] D. Pestov, R. K. Murawski, G. O. Ariunbold, X. Wang, M. Zhi, A. V. Sokolov, V. A. Sautenkov, Y. V. Rostovtsev, A. Dogariu, Y. Huang *et al.*, Optimizing the laser-pulse configuration for coherent Raman spectroscopy, *Science* **316**, 265 (2007).
- [23] Y. J. Lee, S. H. Parekh, J. A. Fagan, and M. T. Cicerone, Phonon dephasing and population decay dynamics of the G-band of

- semiconducting single-wall carbon nanotubes, *Phys. Rev. B* **82**, 165432 (2010).
- [24] K. Kang, T. Ozel, D. G. Cahill, and M. Shim, Optical phonon lifetimes in single-walled carbon nanotubes by time-resolved Raman scattering, *Nano Lett.* **8**, 4642 (2008).
- [25] H. Yan, D. Song, K. F. Mak, I. Chatzakis, J. Maultzsch, and T. F. Heinz, Time-resolved Raman spectroscopy of optical phonons in graphite: Phonon anharmonic coupling and anomalous stiffening, *Phys. Rev. B* **80**, 121403(R) (2009).
- [26] S. Wu, W.-T. Liu, X. Liang, P. J. Schuck, F. Wang, Y. R. Shen, and M. Salmeron, Hot phonon dynamics in graphene, *Nano Lett.* **12**, 5495 (2012).
- [27] L. A. Jakob, W. M. Deacon, O. Hicks, I. Manyakin, O. S. Ojambati, M. Traxler, and J. J. Baumberg, Single photon multi-clock lock-in detection by picosecond timestamping, *Optica* **8**, 1646 (2021).
- [28] H. Hamaguchi and T. L. Gustafson, Ultrafast time-resolved spontaneous and coherent Raman spectroscopy: The structure and dynamics of photogenerated transient species, *Annu. Rev. Phys. Chem.* **45**, 593 (1994).
- [29] S. Mubeen, S. Zhang, N. Kim, S. Lee, S. Krämer, H. Xu, and M. Moskovits, Plasmonic properties of gold nanoparticles separated from a gold mirror by an ultrathin oxide, *Nano Lett.* **12**, 2088 (2012).
- [30] G. Li, Q. Zhang, S. A. Maier, and D. Lei, Plasmonic particle-on-film nanocavities: A versatile platform for plasmon-enhanced spectroscopy and photochemistry, *Nanophotonics* **7**, 1865 (2018).
- [31] R. Chikkaraddy, B. De Nijs, F. Benz, S. J. Barrow, O. A. Scherman, E. Rosta, A. Demetriadou, P. Fox, O. Hess, and J. J. Baumberg, Single-molecule strong coupling at room temperature in plasmonic nanocavities, *Nature (London)* **535**, 127 (2016).
- [32] F. Benz, M. K. Schmidt, A. Dreismann, R. Chikkaraddy, Y. Zhang, A. Demetriadou, C. Carnegie, H. Ohadi, B. De Nijs, R. Esteban *et al.*, Single-molecule optomechanics in “picocavities, *Science* **354**, 726 (2016).
- [33] C. Carnegie, J. Griffiths, B. de Nijs, C. Readman, R. Chikkaraddy, W. M. Deacon, Y. Zhang, I. Szabó, E. Rosta, J. Aizpurua *et al.*, Room-temperature optical picocavities below 1 nm^3 accessing single-atom geometries, *J. Phys. Chem. Lett.* **9**, 7146 (2018).
- [34] G. Di Martino, V. A. Turek, A. Lombardi, I. Szabó, B. de Nijs, A. Kuhn, E. Rosta, and J. J. Baumberg, Tracking nanoelectrochemistry using individual plasmonic nanocavities, *Nano Lett.* **17**, 4840 (2017).
- [35] L. A. Jakob, W. M. Deacon, Y. Zhang, B. de Nijs, E. Pavlenko, S. Hu, C. Carnegie, T. Neuman, R. Esteban, J. Aizpurua *et al.*, Giant optomechanical spring effect in plasmonic nano- and picocavities probed by surface-enhanced Raman scattering, *Nat. Commun.* **14**, 3291 (2023).
- [36] See Supplemental Material at <http://link.aps.org/supplemental/10.1103/PhysRevB.109.195404> for NPoM darkfield scattering, 2pCARS experiments, Fourier transform of Raman spectra, sample stability under pulsed laser illumination, trCARS spectrum detected in single-photon experiments, population and coherence decay of many NPoMs, pulsed SERS and apparent non-equilibrium temperature, exploration of other correlations in fit parameters, power series of time-resolved experiments, decay rates of different vibrations and molecules.
- [37] R. Chikkaraddy, J. Huang, D. Kos, E. Elliott, M. Kamp, C. Guo, J. J. Baumberg, and B. de Nijs, Boosting optical nanocavity coupling by retardation matching to dark modes, *ACS Photon.* **10**, 493 (2023).
- [38] S. Heuke, I. Rimke, B. Sarri, P. Gasecka, R. Appay, L. Legoff, P. Volz, E. Büttner, and H. Rigneault, Shot-noise limited tunable dual-vibrational frequency stimulated Raman scattering microscopy, *Biomed. Opt. Express* **12**, 7780 (2021).
- [39] Y. Wang, C.-Y. Lin, A. Nikolaenko, V. Raghunathan, and E. O. Potma, Four-wave mixing microscopy of nanostructures, *Adv. Opt. Photon.* **3**, 1 (2011).
- [40] M. Danckwerts and L. Novotny, Optical frequency mixing at coupled gold nanoparticles, *Phys. Rev. Lett.* **98**, 026104 (2007).
- [41] D. V. Voronine, A. M. Sinyukov, X. Hua, K. Wang, P. K. Jha, E. Munusamy, S. E. Wheeler, G. Welch, A. V. Sokolov, and M. O. Scully, Time-resolved surface-enhanced coherent sensing of nanoscale molecular complexes, *Sci. Rep.* **2**, 891 (2012).
- [42] N. Hayazawa, T. Ichimura, M. Hashimoto, Y. Inouye, and S. Kawata, Amplification of coherent anti-Stokes Raman scattering by a metallic nanostructure for a high resolution vibration microscopy, *J. Appl. Phys.* **95**, 2676 (2004).
- [43] C. Carnegie, M. Urbieta, R. Chikkaraddy, B. de Nijs, J. Griffiths, W. M. Deacon, M. Kamp, N. Zabala, J. Aizpurua, and J. J. Baumberg, Flickering nanometre-scale disorder in a crystal lattice tracked by plasmonic flare light emission, *Nat. Commun.* **11**, 682 (2020).
- [44] R. C. Maher, C. M. Galloway, E. C. Le Ru, L. F. Cohen, and P. G. Etchegoin, Vibrational pumping in surface enhanced Raman scattering (SERS), *Chem. Soc. Rev.* **37**, 965 (2008).
- [45] J. R. M. Saavedra, A. Asenjo-Garcia, and F. J. García De Abajo, Hot-electron dynamics and thermalization in small metallic nanoparticles, *ACS Photon.* **3**, 1637 (2016).
- [46] H. Wang, K. Ferrio, D. G. Steel, Y. Z. Hu, R. Binder, and S. W. Koch, Transient nonlinear optical response from excitation induced dephasing in GaAs, *Phys. Rev. Lett.* **71**, 1261 (1993).
- [47] M. Hirtschulz, E. Malic, F. Milde, and A. Knorr, Excitation-induced dephasing and ultrafast intrasubband relaxation in carbon nanotubes, *Phys. Rev. B* **80**, 085405 (2009).
- [48] C. Ferrante, A. Virga, L. Benfatto, M. Martinati, D. De Fazio, U. Sassi, C. Fasolato, A. K. Ott, P. Postorino, D. Yoon *et al.*, Raman spectroscopy of graphene under ultrafast laser excitation, *Nat. Commun.* **9**, 308 (2018).
- [49] K. Watanabe, N. Takagi, and Y. Matsumoto, Direct time-domain observation of ultrafast dephasing in adsorbate-substrate vibration under the influence of a hot electron bath: Cs adatoms on Pt(111), *Phys. Rev. Lett.* **92**, 057401 (2004).
- [50] C. B. Harris, R. M. Shelby, and P. A. Cornelius, Effects of energy exchange on vibrational dephasing times in Raman scattering, *Phys. Rev. Lett.* **38**, 1415 (1977).
- [51] C. Artur, E. C. Le Ru, and P. G. Etchegoin, Temperature dependence of the homogeneous broadening of resonant Raman peaks measured by single-molecule surface-enhanced Raman spectroscopy, *J. Phys. Chem. Lett.* **2**, 3002 (2011).
- [52] K. D. Park, E. A. Muller, V. Kravtsov, P. M. Sass, J. Dreyer, J. M. Atkin, and M. B. Raschke, Variable-temperature tip-enhanced Raman spectroscopy of single-molecule fluctuations and dynamics, *Nano Lett.* **16**, 479 (2016).
- [53] H. Arnolds, Vibrational dynamics of adsorbates—Quo vadis? *Prog. Surf. Sci.* **86**, 1 (2011).

- [54] L. A. Jakob, W. M. Deacon, R. Arul, B. de Nijs, N. S. Mueller, and J. J. Baumberg, 2024, [10.17863/CAM.107589](https://doi.org/10.17863/CAM.107589).
- [55] A. Laubereau, D. Von Der Linde, and W. Kaiser, Direct measurement of the vibrational lifetimes of molecules in liquids, *Phys. Rev. Lett.* **28**, 1162 (1972).
- [56] A. Laubereau and W. Kaiser, Vibrational dynamics of liquids and solids investigated by picosecond light pulses, *Rev. Mod. Phys.* **50**, 607 (1978).
- [57] D. Von Der Linde, J. Kuhl, and H. Klingenberg, Raman scattering from nonequilibrium LO phonons with picosecond resolution, *Phys. Rev. Lett.* **44**, 1505 (1980).
- [58] K. T. Tsen, J. G. Kiang, D. K. Ferry, and H. Morkoc, Subpicosecond time-resolved Raman studies of LO phonons in GaN: Dependence on photoexcited carrier density, *Appl. Phys. Lett.* **89**, 112111 (2016).
- [59] R. W. Boyd, *Nonlinear Optics*, 3rd ed. (Academic Press, San Diego, 2007).
- [60] Y. Zhang, J. Aizpurua, and R. Esteban, Optomechanical collective effects in surface-enhanced Raman scattering from many molecules, *ACS Photon.* **7**, 1676 (2020).
- [61] N. S. Mueller, R. Arul, L. A. Jakob, M. O. Blunt, T. Földes, E. Rosta, and J. J. Baumberg, Collective mid-infrared vibrations in surface-enhanced Raman scattering, *Nano Lett.* **22**, 7254 (2022).
- [62] E. Elliott, K. Bedingfield, J. Huang, S. Hu, B. de Nijs, A. Demetriadou, and J. J. Baumberg, Fingerprinting the hidden facets of plasmonic nanocavities, *ACS Photon.* **9**, 2643 (2022).
- [63] F. Benz, R. Chikkaraddy, A. Salmon, H. Ohadi, B. De Nijs, J. Mertens, C. Carnegie, R. W. Bowman, and J. J. Baumberg, SERS of individual nanoparticles on a mirror: Size does matter, but so does shape, *J. Phys. Chem. Lett.* **7**, 2264 (2016).
- [64] J. T. Hugall and J. J. Baumberg, Demonstrating photoluminescence from Au is electronic inelastic light scattering of a plasmonic metal: The origin of SERS backgrounds, *Nano Lett.* **15**, 2600 (2015).